INTERNATIONAL JOURNAL OF RESEARCH AND TECHNOPRENEURIAL INNOVATIONS
(IJRTI)

P-ISSN: 3043-5722; E-ISSN: 3141-270X
Volume 3 Issue 2 (October 2026)
Central Instrument Laboratory, University of Port Harcourt, Nigeria
E-mail: centralinstumentlaboratory@uniport.edu.ng
Website: www.ijrti.com.ng; https://ciluniport.com.ng/

Computational Exploration of Structural, and Stabilities, Electronic, Optical and Photocatalytic Properties in Rare-sulfides Containing Halides YSX (X = F, and Br)

Abdu Barde[1,*], Daniel Joubert[2], Bashir Muhammad[1], Abdulsalam Kawu Ahmed[3], Adamu Baba Wada[4], Shamsuddeen Hashim Yusuf[5], Idris malam Bala[1]

DOI: https://doi.org/10.60787/ijrti.vol3no2.90

[1]Department of Technical and Vocational Education, Jigawa State Polytechnic, Dutes, Nigeria

[2]School of Physics, University of the Witwatersrand, Johannesburg, South Africa

[3]Department of Physics, Federal University of Kashere, Gombe State, Nigeria

[4]Department of Mechanical Engineering Technology, Jigawa State Polytechnic, Dutse, Nigeria

[5]Department of Science Laboratory Technology, Jigawa State Polytechnic, Dutse, Nigeria

Email address:

[*]Corresponding author: abdubarde@jigpoly.edu.ng

Dates: Received: 25 September 2026; Revised: 14 October 2026; Accepted: 21 October 2026.

To cite this article:
Barde, A., Joubert, D., Muhammad, B., Ahmed, A.K., Wada, A.B., Yusuf, S.H., Bala, I.M. Computational Exploration of Structural, and Stabilities, Electronic, Optical and Photocatalytic Properties in Rare-sulfides Containing Halides YSX (X = F, and Br). *International Journal of Research and Technopreneurial Innovations*, 2026; 3(2): 32-45

Keywords:
YSX,
Halide,
Photocatalytic

ABSTRACT

This study explores YSX (X = F, Br), a rare-earth sulfide-halide compound, as a photocatalytic material for hydrogen renewable energy using density functional theory (DFT) with the projector-augmented-wave (PAW) method and a meta-GGA potential. Structural relaxations using the PBE functional yielded lattice parameters of a = b = 3.73443 Å and c = 6.77194 Å, and unit-cell volume (V = 94.44 Å3) for tetragonal YSF, and a = 6.66456 Å, b = 6.81165 Å, and c = 13.07640 Å, and (V = 593.62 Å3) for orthorhombic YSBr. We tested the stability of these compounds using elastic and phonon stability, and confirmed that both are mechanically and dynamically stable. Electronic band structures calculated with the TB-mBJ potential reveal direct band gaps of 2.06 eV and 2.54 eV for YSF and YSBr at the gamma point, respectively, and indicate that the compounds are semiconductors. Optical property calculated from HSE06+BSE further reveal the semiconductor characteristic by YSF 2.22 eV and YSBr 2.59 eV reported Tauc plot optical gaps. The calculated electron effective mass (Me) is 0.30 me and 0.59 me, and the hole effective mass (Mh) is 1.89 me and 1.17 me, revealing good electron and moderate hole mobility for YSF and YSBr, respectively. Calculated conduction and valence band-edge ECB +0.30 V, -0.48 V, and EVB +2.52 V, +2.12 V for YSF and YSBr, respectively, indicated that YSBr is thermodynamically feasible for photocatalytic water splitting.

1. INTRODUCTION

The development of efficient photocatalysts for solar-driven water splitting is an important challenge in renewable energy research. Photocatalytic water splitting provides a route for converting solar energy into chemical energy through the generation of hydrogen and oxygen. In

semiconductor photocatalysts, photo-excited electrons participate in the hydrogen evolution reaction (HER), while photogenerated holes drive the oxygen evolution reaction (OER) [1], [2]. The overall water-splitting reaction has a minimum thermodynamic potential of 1.23 V under standard conditions. In practical systems, additional overpotentials are required to overcome the kinetic barriers associated with the HER and OER [3]. Therefore, the development of efficient photocatalysts requires simultaneous consideration of optical absorption, electronic structure, band edge positions, charge-carrier separation, and structural stability. Incorporate the applicable criteria that follow.

For overall water splitting, the conduction-band minimum (CBM) must be sufficiently negative to drive proton reduction, while the valence-band maximum (VBM) must be sufficiently positive to facilitate water oxidation. Thus, the band edges should appropriately straddle the water redox potentials. An appropriate band gap is also necessary for effective solar absorption. Although the thermodynamic energy requirement corresponds to a band gap of approximately 1.23 eV, practical photocatalysts generally require larger band gaps because of overpotentials and other energy losses [3]. Consequently, semiconductors with band gaps in or near the visible-light region are of considerable interest for solar-driven photocatalysis.

Beyond the band gap, photocatalytic performance depends strongly on the generation, separation, and transport of photogenerated charge carriers. Efficient separation of electrons and holes is necessary to minimize recombination before the carriers reach the surface reaction sites. Rapid electron–hole recombination can reduce the concentration of carriers available for the HER and OER and consequently decrease photocatalytic activity [4]. Structural and chemical stability are also important for maintaining the integrity of the photocatalyst during operation. These requirements have motivated extensive theoretical and experimental investigations of semiconducting materials, including layered and two-dimensional systems, whose structural dimensionality can lead to tunable electronic properties and strong light–matter interactions [3].

Rare-earth-containing chalcogenides have attracted attention due to their diverse structural chemistry and tunable electronic properties [3]. Recent studies have demonstrated that yttrium-based sulfides are promising candidates for photocatalytic water splitting. Barde et al. [5] investigated Y2S3 and the Janus compound Y2TeS2, finding HSE06 band gaps of 2.75 eV and 2.70 eV, with band-edge positions suitable for both the hydrogen and oxygen evolution reactions. Kawu et al. [6] reported Sc8S12 and Sm8S12 as visible-light photocatalysts, with mBJ band gaps of 1.6 eV and 1.4 eV, respectively, and favorable effective masses for charge transport.

Recent first-principles studies have extended this search to rare-earth chalcogen-halide and chalcohalide materials. Yttrium-containing compounds have attracted attention n because of their diverse structural and electronic properties. For example, monolayer Y2T2I2 has been investigated as a potential photocatalyst [7], while monolayer YTeI has also been reported to exhibit electronic and optical characteristics relevant to solar-driven water splitting [8]. These studies suggest that yttrium-based chalcogen-halide compounds provide an interesting materials platform for investigating photocatalytic properties. Yttrium-based sulfides provide an opportunity to examine how halide composition influences the structural and electronic properties of rare-earth-containing materials. In this study, the compounds are represented by YSF and YSBr are investigated. The replacement of fluorine by the larger bromine anion can alter the lattice dimensions, crystal symmetry, bonding environment, and electronic structure. YSF adopts a tetragonal structure, whereas YSBr has an orthorhombic structure. The

different crystal structures therefore provide a useful basis for examining the influence of halide composition on the structural, mechanical, dynamical, and electronic properties of these materials. Despite the growing interest in yttrium-containing chalcogen-halide materials, systematic studies of the structural, mechanical, dynamical, and electronic properties of bulk YSF and YSBr remain limited. In particular, mechanical and dynamical stability must be established before their photocatalytic properties can be considered in detail. Mechanical stability can be evaluated from the elastic constants and the corresponding Born stability criteria, whereas dynamical stability can be assessed from the phonon spectrum. Electronic structure calculations can subsequently provide information on the band-gap magnitude and nature, which are important for assessing the potential for solar-light absorption. In the present work, we perform a comprehensive first-principles investigation of YSF and YSBr using density functional theory (DFT). The structural properties are determined following full structural relaxation, while the mechanical stability is evaluated from the calculated elastic constants and Born stability criteria. Phonon calculations are performed to examine dynamical stability. The electronic structures are investigated using the Perdew - Burke - Ernzerhof functional PBE [9] and modified Becke–Johnson (mBJ) [10] potentials to obtain improved estimates of the semiconductor band gaps. Optical properties of YSF and YSBr and optical gap (Eg) with a particular attention is given to the band-gap characteristics and their implications for visible-light absorption. The results provide a systematic assessment of the structural, mechanical, dynamical, and electronic properties of YSF and YSBr and establish a basis for further investigation of their band edge alignment, optical properties, and thermodynamic feasibility of photocatalytic performance. The study is based on theoretical DFT computational method to predict new rare-earth sulfide-halide material YSF, and

YSBr that exhibits a photocatalytic feasibility for use in energy conversion application. The work focuses on Structural properties, mechanical and dynamical stabilities, electronic and optical properties of YSF and YSBr with a view to providing value information to feasibility for photocatalytic applications.

2. MATERIALS AND METHOD

2.1. Computational Method

First-principles calculations were carried out to investigate the structural, electronic, optical properties, and thermodynamic feasibility and photocatalytic properties of YSF and YSBr, with particular emphasis on the effect of halogen substitution in rare-earth Yttrium-based sulfides. All simulations were performed within the framework of density functional theory (DFT) as implemented in the Vienna Ab-initio Simulation Package (VASP) [11, 12]. The exchange - correlation interaction was described using the Perdew - Burke - Ernzerhof functional revised for solids (PBE) [9]. The interaction between ion cores and valence electrons was treated using the projected augmented wave (PAW) method [13], and the electronic wave functions were expanded in a plane-wave basis set.

Brillouin zone integrations were performed using the Monkhorst - Pack scheme [14]. K-point meshes of 7 × 7 × 4 and 5 × 5 × 2 were employed for YSF and YSBr, respectively. A plane-wave cutoff energy of 520 eV was adopted to ensure convergence of total energies and forces. Structural optimization was carried out until the total energy and ionic forces were well converged. In the absence of reported elastic and vibrational data for these systems, phonon properties were evaluated using the PHONOPY package [15], which employs the finite displacement method. The elastic constants were computed from the

optimized structures using the Lagrangian formulation of elasticity [16], where the stress–strain relationship

is expressed in terms of symmetric second-rank tensors. Electronic structure calculations, including band structures and band gaps, were obtained using both self-consistent and non-self-consistent approaches [17]. In addition to PBE, the modified Becke–Johnson (mBJ) potential [10] was employed to improve the accuracy of band gap predictions.

The hybrid Heyd-Scuseria-Ernzerhof (HSE06) functional [18] was employed to evaluate the Green's function (G0W0), and static dielectric constant for optical property analysis, and to take account of excitonic effects, the optical absorption spectra from the Green's function G0W0 together with the Bethe- Salpeter equation (BSE) [19]. The positions of the optical band gap were determined using Tauc plots [20]. The band edge positions were estimated using Mulliken's electronegativity concept [21], and a semiconductor-based method equation [22], together with the calculated optical band gap, to determine the photocatalytic feasibility of YSF and YSBr.

3. RESULTS AND DISCUSSION

3.1. Structural Properties

To our knowledge, there are no experimental or theoretical studies to compare our results; the structures of YSF and YSBr are fully relaxed, and the structural parameters of YSF and YSBr are summarized in Table 1. YSF adopted a tetragonal structure with a = b = 3.73 Å and c = 6.77 Å, resulting in a unit-cell volume of 94.44 Å^3. YSBr crystallizes in an orthorhombic structure with a = 6.66 Å, b = 6.81 Å, and c = 13.08 Å, giving a unit-cell volume of 593.62 Å^3.

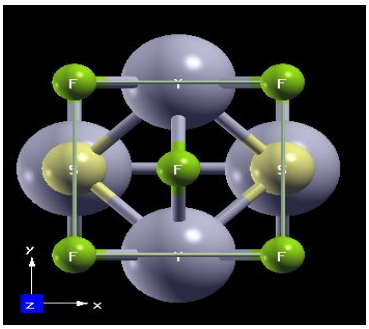


Figure 1. *The relaxed crystal structure of YSF*

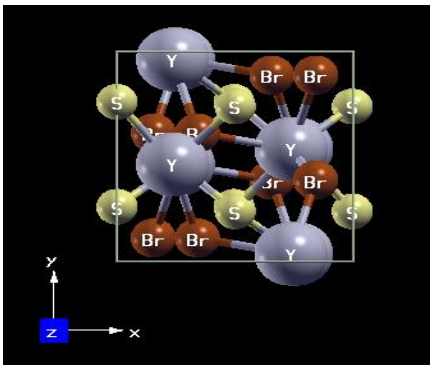


Figure 2. *Relax Crystal Structure for YSBr.*

Table 1. *The relaxed crystal structure type, lattice parameters, angles, and volumes*

Parameters	**YSF**	**YSBr**
Crystal	Tetragonal	Orthorhombic
a (Å)	3.73	6.66
b (Å)	3.73	6.81
c (Å)	6.77	13.08
α=β=γ (^{0})	90	90
V (Å^3)	94.44	593.62

The structural relaxation was verified by examining the resulting stress tensor. For both compounds, all diagonal and off-diagonal stress components converged to below 0.001 kB, while the calculated Pulay stress was negligible. The stress symmetry is also consistent with the assigned crystal systems. The YSF exhibits a

lattice with a = b ≠ c, which is consistent with tetragonal symmetry. In contrast, YSBr exhibits a ≠ b ≠ c, consistent with orthorhombic symmetry.

The substantially larger unit-cell volume of YSBr compared with YSF can be associated, in part, with the larger ionic radius of Br− compared with F−; other studies verify this trend [23, 24]. The larger anion therefore produces a more expanded crystal structure, as indicated by the lattice parameters and unit cell volume as shown in Table 1; YSBr has larger parameters compared to YSF.

3.2. Mechanical Stability

The mechanical stability of a crystal can be assessed using the Born stability criteria [19] for tetragonal YSF and orthorhombic YSBr materials, which require the elastic energy to remain positive under arbitrary small homogeneous strains. The calculated elastic constants C_{ij} for YSF and YSBr are listed in Table 2.

***Table 2**: Calculated elastic constants C_{ij} in Giga Pasca (GPa) for YSF and YSBr*

Elastic constants	YSF	YSBr
C_{11}	200.56	112.09
C_{22}	200.56	134.48
C_{33}	191.21	95.25
C_{12}	77.58	44.89
C_{13}	76.34	40.87
C_{23}	76.34	47.80
C_{44}	61.72	41.14
C_{55}	61.72	38.80
C_{66}	83.18	27.99

For tetragonal YSF the Born stability criteria are given by [20] stated that:

$$C_{11} > |C_{12}|,$$
$$2C^2_{13} < C_{33}(C_{11} + C_{12}),$$
$$C_{44} > 0, \qquad C_{66} > 0 \qquad (1)$$

Similarly, for the orthorhombic YSBr, the Born stability criteria are [19] stated that:

$$C\ 11 > 0,$$
$$C_{11}C_{22} > C^2_{12},$$
$$C_{11}C_{22}C_{33} + 2C_{12}C_{13}C_{23} - C_{11}C^2_{23} - C_{22}C^2_{13} - C_{33}C^2_{12} > 0,$$
$$C_{44} > 0, \qquad C_{55} > 0, \qquad C_{66} > 0. \qquad (2)$$

Substitution of the calculated elastic constants in (1) and (2) above confirmed the mechanical stability of YSF and YSBr, respectively.

The bulk modulus (B), shear modulus (G), Young's modulus (E), and Poisson's ratio (ν) were calculated using the Voigt–Reuss–Hill (VRH) approximation [25, 26, 27] properties measure the material's response to external pressure and evaluate whether the material is ductile or brittle. The corresponding Voigt, Reuss, and Hill averages are presented in Table 3.

***Table 3**: Calculated Bulk, Shear, and Young Modulus in Giga Pascal (GPa), Poisson's, and B/B ratio for YSF and YSBr*

Parameters	Method	YSF	YSBr
Bulk modulus B (GPa)	Voigt	116.99	67.66
	Reuss	116.92	66.10
	Hill	116.95	66.88
Shear modulus G (GPa)	Voigt	65.46	35.47
	Reuss	64.44	34.44
	Hill	64.95	34.96
Young's modulus E (GPa)	Viogt	165.51	90.58
	Reuss	163.31	88.04
	Hill	164.41	89.31
Poisson's ratio, ν	Viogt	0.26	0.28
	Reuss	0.27	0.28
	Hill	0.27	0.28
B/G ratio	Hill	1.80	1.91

The Pugh ratio, B/G, is the ratio of Bulk modulus (B) to the shear modulus (G) and was used as an empirical indicator of the ductile–brittle tendency of the compounds proposed by Pugh [29].

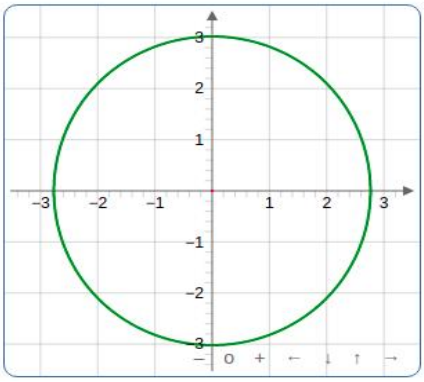
According to the commonly used Pugh criterion, the calculated B/G ratio from the Voigt relations of YSF 1.80 and YSBr 1.91 are greater than the reference value of 1.75; hence, both YSF and YSBr materials' properties fall within the ductile regime, where, when a tensile stress is applied to a ductile material, it undergoes plastic deformation before breaking.

The calculated elastic moduli show that YSF has larger bulk, shear, and Young's moduli than YSBr. This difference indicates that YSF would demonstrate greater resistance to volume change, shear deformation, and tensile deformation. The difference is consistent with the more compact structure of YSF and the different chemical environment associated with the smaller fluorine anion, although a direct assessment of bond strength would require additional bonding analysis.

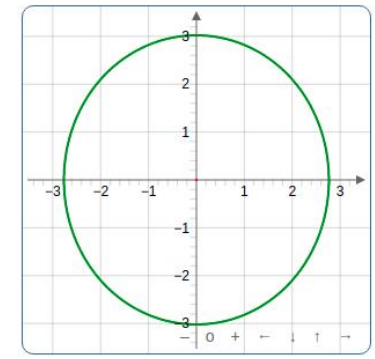
The Poisson's ratios calculated from the Hill approximation are 0.27 for YSF and 0.28 for YSBr, respectively. The calculated Poisson's ratios are greater than 0.26, a borderline between brittle and ductile materials; in comparison, 0.27 and 0.28 are greater than 0.26, which further confirms the ductile behavior of YSF and YSBr. From the calculated Poisson's ratio, both materials are associated with metallic bonding.

3.2.1. Elastic Anisotropy

The directional dependence of the elastic properties was visualized using three-dimensional representation surfaces generated with ELATE [30]. The spatial dependence of the linear compressibility of YSF (tetragonal), and YSBr (orthorhombic) is presented in Figures 3 and 4. The linear compressibility is defined as the ratio of the induced stretch along a given line under pressure.



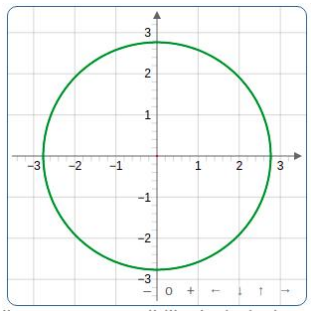
(a)

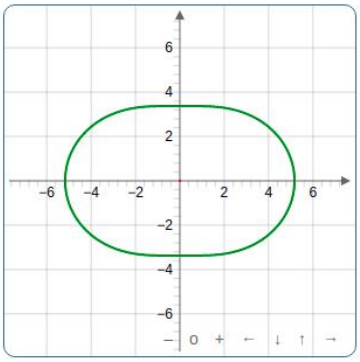


(b)

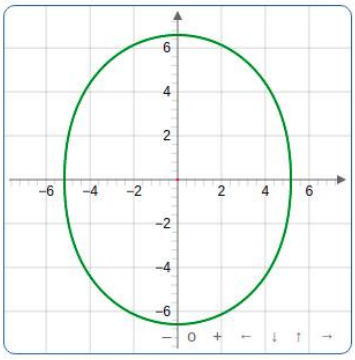
(c)

Figure 3. *The YSF spatial dependence of linear compressibility in (a) xy, (b) xz, and (c) yz planes*

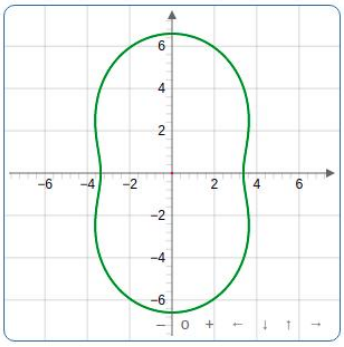




(a)



(b)



(c)

Figure 4. *The YSBr spacial dependence of linear compressibilityin (a) xy, (b) xz, and (c) yz planes*

Except for isotropic cubic materials where $A^U = 0$, all other anisotropic materials have $A^U > 0$. For both YSF and YSBr, the linear compressibility has a directional dependence along the two planes; the xy-plane and xz and yz planes are shown in Figures 3 and 4. Our calculation confirmed the spatial dependence of linear compressibility as shown in Figures 3 and 4, and calculated the elastic constants C_{11}, C_{22}, and C_{33}, showing that YSF and YSBr are anisotropic materials.

The characteristic anisotropy of YSF and YSBr was further confirmed by calculating the universal elastic anisotropy index, A^U, and shear anisotropy factor, A_G. For YSF, the calculated values of A^U and A_G are 0.080 and 0.008, whereas for YSBr, they are 0.17 and 0.015, respectively. In comparison, YSF has smaller values of both universal anisotropy and the shear anisotropic factor than YSBr. For an isotropic material, $A^U = 0$, and the greater the value from zero, the greater the extent of elastic anisotropy of the material. Hence, the calculated A^U

and A_G further justified the characteristic elastic anisotropy of YSF and YSBr, and that YSBr is more anisotropic than YSF.

3.3. Dynamic Stability

The dynamical stability of YSF and YSBr was assessed by calculating their phonon dispersion relations using the finite-displacement method implemented in Phonopy [15]. The force constants were obtained from first-principles calculations; the forces were determined from the supercells containing finite atomic displacements, as shown in Table 4.

Table 4: *Calculated phonon properties of YSF and YSBr*

Properties	**YSF**	**YSBr**
Imaginary modes	None	None
Acoustic sum rule violation at gamma (Γ)	< 0.01 THz	< 0.01 THz
Maximum phonon frequency	13.3 THz	10.5 THz
Maximum frequency	444 cm^{-1}	350 cm^{-1}
Acoustic–optical gap	None	None
Dynamical stability	Confirmed	Confirmed

Presented in Figures 5 and 6 are the phonon dispersions; the frequencies are the product of the real displacements along the Brillouin zone of the YSF and YSBr compounds. From Figures 5 and 6, the results show that there are no imaginary frequency modes are observed along the Brillouin

zone observed respectively. This result confirms the dynamical stability of the tetragonal YSF and YSBr orthorhombic structures. The phonon frequency response is characterized by acoustic and optical modes; for YSF, the three acoustic branches approach zero frequency at the Γ point, which is consistent with the acoustic sum rule. The lower acoustic modes are the product of Yttrium (Y) vibration, as shown in Figure 5, right panel. The

optical branches extend from approximately 2 THz to a maximum frequency of approximately 13.3 THz, corresponding to about 444 cm −1. The higher frequency modes are predominantly associated with vibrations involving the lighter fluorine (F) and Sulfur (S) atoms, as indicated by the PDOS in Figure 5 (right panel).
Similarly, for YSBr, the three acoustic branches

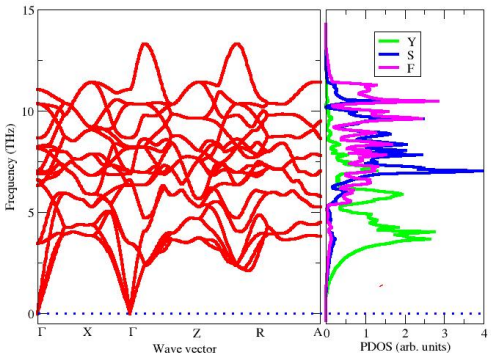


Figure 5. *The YSF phonon dispersion frequencies (left panel) and the partial density of state (PDOS) from the (right panel)*

approach zero frequency at the Γ point, consistent with the acoustic sum rule, and are attributed to Y and Br atomic vibrations, as indicated in the PDOS right panel of Figure 6. For the optical mode, the maximum phonon frequency is approximately 10.5 THz, corresponding to about 350 cm −1, and the upper optical mode frequencies were predominantly due to the vibration of sulfide (S) and Yttrium-based (Y) atoms. The results of the dynamical stability further confirmed the dynamic stability of YSF and YSBr materials and are consistent with the mechanical stability established from the Born criteria.

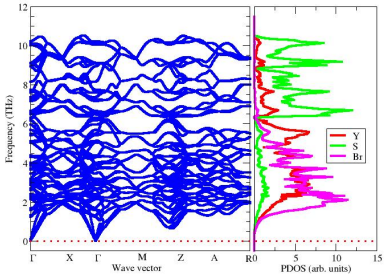
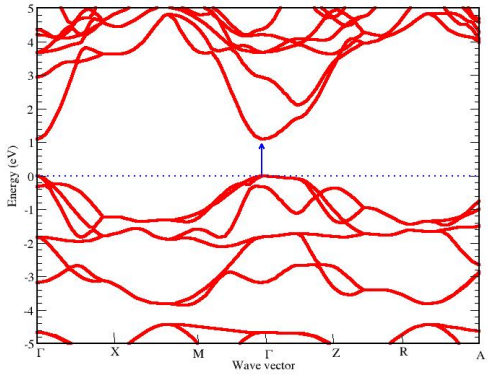


Figure 6. *The YSBr phonon dispersion frequencies (left panel) and the partial density of state (PDOS) from the (right panel)*

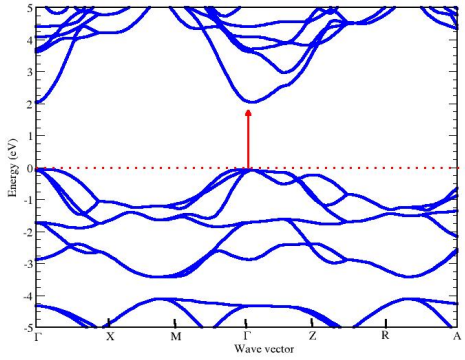
3.4. Electronic Properties

The electronic band structures of YSF and YSBr were calculated using both the PBE exchange–correlation functional [12] and the modified Becke–Johnson (mBJ) potential [24]; mBJ was employed because PBE underestimated the band gap. For rare-earth-containing sulfides, mBJ was found to describe their band gap accurately [25]; the calculated band structures provide information on the electronic character, band-gap magnitude, and nature of the fundamental transitions in the two compounds. The PBE band structure of YSF exhibits a direct band gap of 1.06 eV at the Γ point as shown in Figure 7(a). With the application of the mBJ potential, the mBJ potential significantly improved the band gap from 1.06 eV to 2.06 eV while retaining its direct character at Γ, as indicated in Figure 7(b). This approximate improvement of 1.00 eV demonstrates the substantial effect of the mBJ potential in modifying the fundamental gap. The partial density of states (PDOS) indicates that the upper valence-band states are dominated

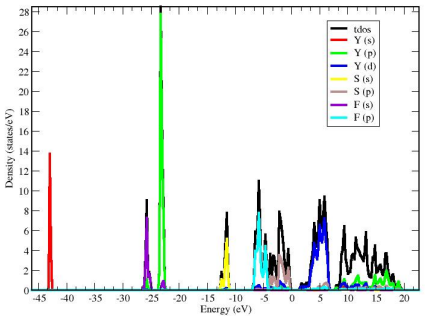
primarily by Y (d) orbitals. In YSF, far below the valence band, -5 eV has a substantial contribution from S (p) states and F (p) states. Similarly, the lower conduction band revealed a strong contribution from Y(p) states.



(a)



(b)

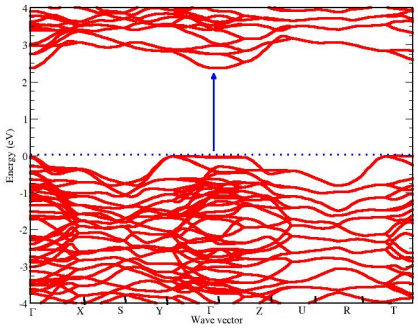


(c)

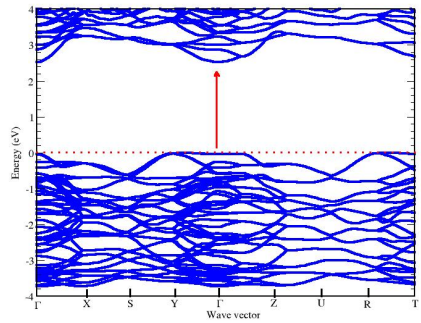
Figure 7. *The YSF electronic band structure calculated from (a) DFT, (b) mBJ, and (c) mBJ partial density of state (PDOS)*

Similarly, for the YSBr compound, the calculated PBE band structure exhibits a direct band gap at the gamma (Γ) point, and the mBJ calculation adopted a similar direct band gap structure, as shown in Figure 8 (a) and (b). The measured PBE band gap was 2.30 eV, and 2.54 eV for the mBJ functional.

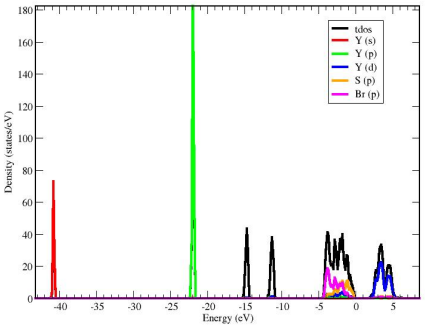
Analysis of the mBJ partial density of states (PDOS) shown in Figure 8 (c) revealed that the lower conduction band (CB) was dominated by Y (d) contribution, while in the upper valence band (VB) a hybridization of Br (p), S (p), and Y (d) was observed, with predominant contribution from Br (p) and S (p).



(a)



(b)



(c)

Figure 8. *The YSF electronic band structure calculated from (a) DFT, (b) mBJ, and (c) mBJ partial density of state (PDOS)*

The fundamental gap calculated with the mBJ potential revealed that both YSF and YSBr are

semiconductors and can absorb light in the visible region, in comparison with our previous study of rare earth chalcogenide Y2S3 and Y2TeS2 [5], the inclusion of halides F and Br in the structural network of rare earth chalcogenides modifies its structural and electronic properties. To assess the potential of YSF and YSBr for energy conversion applications, in addition to the calculated fundamental gap, we calculated the carrier effective masses. The carrier effective masses M_e and M_h, derived from the curvature of the band structure, are one of the factors in assessing a semiconductor material's charge transport and carrier mobility, which is consequently important in photocatalysis and thermoelectric energy conversion. The calculated fundamental gap and the carrier effective mass are depicted in Table 5.

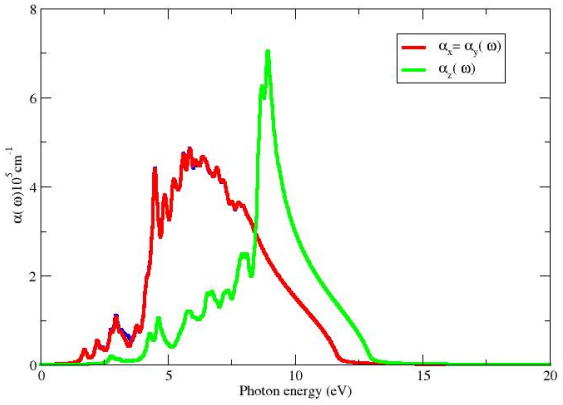
Table 5: *The YSF and YSBr calculated fundamental gap (E_g), and the effective carrier mass respectively*

Properties	**YSF**	**YSBr**
PBE gap (E_g)	1.06 eV	2.30 eV
MBJ gap (E_g)	2.06 eV	2.54 eV
Transition type	Direct	Direct
Electron effective mass (M_e)	$0.30m_e$	$0.59m_e$
Hole effective mass (M_h)	$1.89m_e$	$1.17m_e$

The possession of lower electron effective mass (0.30 me and 0.59 me for YSF and YSBr, respectively suggests that both materials would have the potential to exhibit higher electron mobility and better electron transport. Higher values of hole effective mass (1.89 me and 1.17 me for YSF and YSBr, respectively suggest a moderate hole transport, for electron-hole diparity the YSF and YSBr possess a pronounced electron – hole effective mass asymmetry with YSBr having a reduced electron – hole mass disparity.

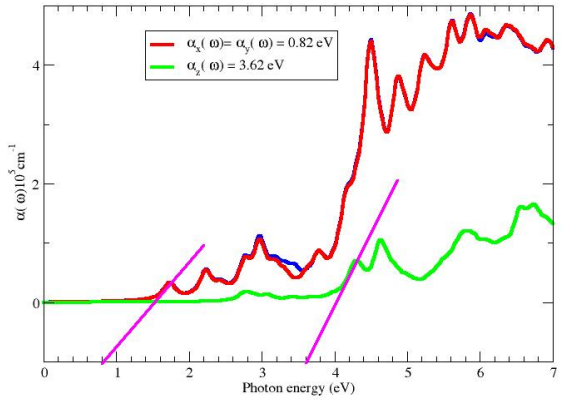
3.4.1. Optical property

The optical properties of YSF and YSBr were investigated to elucidate their potential for photocatalytic applications, where the feasibility depends on the material's optical band gap, and to determine the influence of halide incorporation on the optical response of yttrium-based sulfides. The frequency-dependent complex dielectric function $\varepsilon(\omega) = \varepsilon1(\omega) + i\varepsilon2(\omega)$ was used to determine the principal optical parameters, including the absorption coefficient. The calculated optical absorption obtained using the HSE06 approach presented in Figure 9.

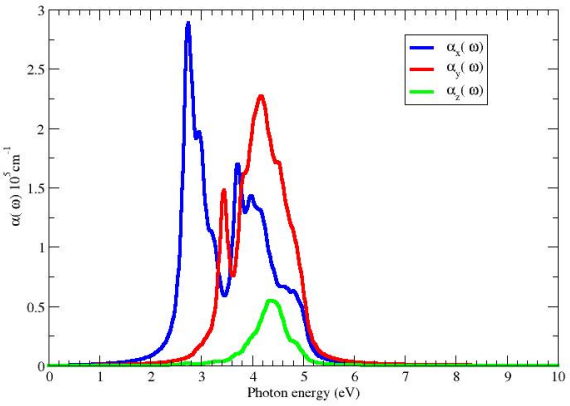


(a)

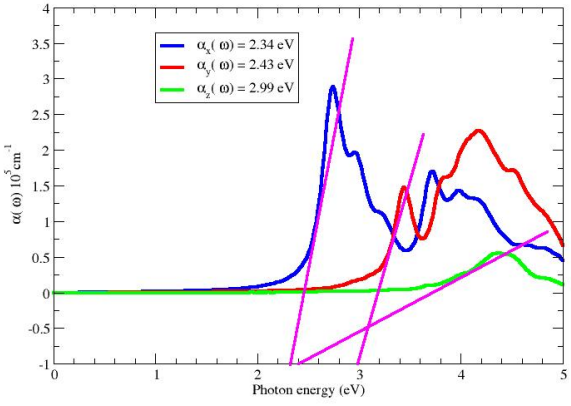
***Figure 9**. Absorption spectra and Tauc plot fitting the linear region to evaluate the band gap at x-intercept from HSE06+BSE for YSF (a), (b), and YSBr (c), and (d), respectively*



(b)



(c)



(d)

For YSF, a tetragonal, the onset principal optical-response energies obtained from the α(ω) spectra are 0.82 and 3.62 eV along the x=y and z directions, respectively, while for YSBr, orthorhombic, the corresponding characteristic absorption energies are 2.32, 2.43, and 2.99 eV along the x, y, and z directions, respectively.
The Tauc plot in Figure 9 (c) and (d) shows the linear extrapolation of the absorption spectra of YSF and YSBr to evaluate the band gaps. Tauc

method [36] linearly extrapolates the absorption edge from:

$$\alpha h\nu = K(h\nu - E_g)^n \quad (3)$$

where α is absorption, h ν is photon energy, K is the proportionality constant, Eg is the absorption gap, and n defines the type of transition, n equal to 1/2 for indirect and 2 for direct transition, respectively. The derived absorption band gap, taken from the average of Tauc plots of the onset crystallographic directions, is consistent with our band structure calculations: a direct transition gap of 2.22 eV for YSF (Tetragonal) and 2.59 eV YSBr (orthorhombic). These values indicate that YSF is characterised by optical transitions in the visible region of green 559 nm, whereas the dominant optical response of YSBr extends into the blue region corresponding to approximate wavelength of 479 nm. No resported experimental and theoritcal work to compare but progressive blue shift of the optical response from YSF to YSBr is consistent with other calculations [31, 32] of the increase in their calculated transition band gaps and demonstrates the important role of halide substitution in tuning the optical response.

3.4.2. Photocatalytic properties

We assess the implication of the calculated optical gap and the carrier effective mass of YSF and YSBr to photocatalytic application. The optical band gaps of 2.22 eV for YSF and 2.59 eV for YSBr indicate that both compounds can absorb radiation in the visible-light region, the calculated electron effective mass of $0.30m_e$ and $0.59m_e$ respectively were found favorable for higher electron mobility. This characteristic can facilitate strong interband optical transitions and may therefore be beneficial for light absorption [33].

The assessment of YSF and YSBr for photocalalytic thermodynamic feasibility requires the optical gap, electronegativities of the individual compound, and the calculation of band-edge potentials for water splitting. The concept of

Mulliken electronegativity was employed to calculate the band edges via the equation:

$$E_{CB} = \chi - E_e - 0.5E_g \quad (4)$$

$$E_{VB} = E_{CB} + E_g \quad (5)$$

where E_{VB} and E_{CB} are the valence band and conduction band edges, electronegativity, and Ee = 4.5 eV is the free-electron hydrogen energy scale, and E_g is the averages of optical gap deduced from Tauc plot. The calculated electronegativities for YSF and YSBr are 5.91 eV and 5.32 eV, respectively.

The calculated band edges according to (3) and (4) are E_{CB} = +0.30 V, E_{VB} = +2.52 for YSF, and E_{CB} = -0.48 V, E_{VB} = +2.12 V for YSBr, respectively. It is evident from Figure 9 that YSBr has a sufficient band edge potential that aligns with the normal hydrogen electrode (NHE), the reduction potential (purple) dotted line, and the oxidation potential (green) dotted line; the conduction band -0.48 V is more negative to the hydrogen reduction potential (0.00 V), and the valence band +2.12 V is more positive to the oxidation potential (1.23 V), straddling the redox reaction for the evolution of hydrogen and oxygen.

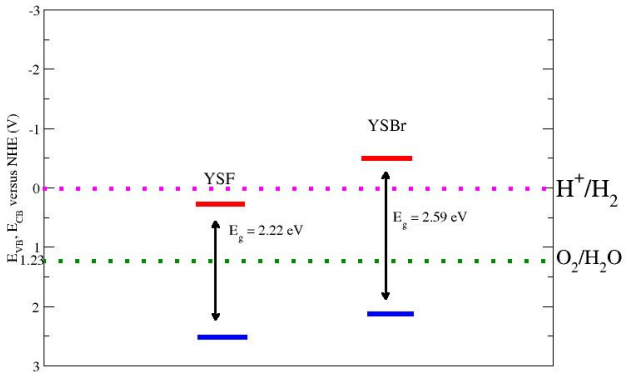


Figure 10. *The YSF and YSBr calculated band edges the E_{CB} and E_{VB} in comparison with the reduction potential H^+/H_2 and the oxidation potential O_2/H_2O at pH = 0*

Similarly, for YSF, the calculated conduction band edge of +0.30 V is below the hydrogen reduction potential and hence does not have the required

reduction potential, but has the required oxidation potential of +2.44 V compared to the standard (1.23 V) oxidation potential. Hence, YSF has only the required oxidation potential for the redox reaction for the feasibility of oxygen evolution.

4. Conclusions

The density functional theory within PAW with a meta-GGA functional was successfully used to explore the thermodynamic suitability of YSX (X = F and Br) for photocatalytic water splitting applications. The Born criterion revealed the elastic stability, and evidence from Figures 5 and 6 revealed the dynamic stability of YSX (X = F, and Br). Also, Figures 7 and 8 show that YSX (X = F and Br) are semiconductors with 2.06 eV and 2.54 eV band gaps, optical band gap average from Tauc plot reveal that YSF and YSBr has band gap of 2.22 eV and 2.59 eV consistent with band structure calculation, the calculated band gaps are capable of absorbing visible light. The calculated effective mass and conduction and valence band edges in Figure 10 revealed that YSBr is a semiconductor with a suitable band gap, effective mass, and band edges that are thermodynamically feasible for photocatalytic water-splitting applications.

Acknowledgements

We extend our appreciation to Jigawa State Polytechnic, Dutse, for the Institutional Research Grant (IBR) for the year 2026. We like to acknowledge the Centre for High-Performance Computing (CHPC), South Africa, for providing computational resources for this work.

Conflict of Interest Declaration

The author(s) declare no conflicts of interest.

References

[1] Fujishima, A. and Honda, K. (1972) Electrochemical photolysis of water at a semiconductor electrode. *Nature,* **238**, 37–38.

[2] Walter, M. G., Warren, E. L., McKone, J. R., Boettcher, S. W., Mi, Q., Santori, E. A., and

Lewis, N. S. (2010). Solar water splitting cells. *Chemical reviews*, ***110*** 6446-6473.

[3] Nishioka, S., Osterloh, F. E., Wang, X., Mallouk, T. E., and Maeda, K. (2023). Photocatalytic water splitting. *Nature Reviews Methods Primers*, **3** 42.

[4] Fu, H., Wu, Y., Guo, Y., Sakurai, T., Zhang, Q., Liu, Y., and Wang, P. (2025). A scalable solar-driven photocatalytic system for separated H2 and O2 production from water. *Nature Communications*, **16** 990.

[5] Barde, A., Kawu, A. A., & Mohammed, H. A. H. (2025). Numerical Simulation and Evaluation of Y2 S3 and Y2 TeS2 on Structural, Stability, and Electronic Properties for Photocatalytic Water Splitting Applications. J. Energy Res. Rev., **17**, 1–13.

[6] Kawu, A. A., Suleiman, A. B., Abdullahi, S. S., Barde, A., Alrahili, M. R, and Itas, Y. S. (2026). Density Functional Theory Study of Sc8S12 and Sm8S12 as Photocatalysts for Water Splitting. *Computational Condensed Matter*, **e01313**.

[7] Mao, D., Wan, R., Wang, S., Zhang, Z., Li, M., Tian, G., & Chen, S. (2025). Monolayer YTeI for photocatalytic water splitting. *Applied Surface Science*, ***710***, 163928.

[8] Wang, S., Wan, R., Zhang, Z., Li, M., & Tian, G. (2025). Design and evaluation of Y2Te2I2 monolayer: A promising 2D photocatalytic water splitter. *International Journal of Hydrogen Energy*, ***106***, 1066-1075.

[9] Perdew, J. P., Burke, K., and Ernzerhof, M. (1996). Generalized gradient approximation made simple. *Physical review letters*, *77*, 3865.

[10] Koller, D., Tran, F., and Blaha, P. (2011). Merits and limits of the modified Becke-Johnson exchange potential. *Physical Review B—Condensed Matter and Materials Physics*, ***83***, 195134.

[11] Kresse, G., & Furthmüller, J. (1996).

Efficient iterative schemes for ab initio total-energy calculations using a plane-wave basis set. *Physical review B*, ***54***, 11169.

[12] Kresse, G., Marsman, M., and Furthmüller, J. (2014). Vienna Ab-Initio Package Vienna Simulation: VASP the GUIDE. *VASP Man*, *237*.

[13] Kresse, G., and Joubert, D. (1999). From ultrasoft pseudopotentials to the projector augmented-wave method. *Physical review b*, ***59***, 1758.

[14] Monkhorst, H. J. and Pack, J. D. (1976). Special points for Brillouin-zone integrations. *Physical review B, 13,* 5188.

[15] Togo, A. (2009). Phonopy http://phonopy.sourceforge.Net.

[16] Wallace, D.C., Callen, H., 1972. Thermodynamics of crystals. *American Journal of Physics,* **40**, 1718 – 1719

[17] Jones, R.O., Gunnarsson, O., 1989. The density functional formalism, its applications and prospects. *Reviews of Modern Physics,* **61**, 689

[18] Heyd, J., Scuseria, G.E., Ernzerhof, M., 2003. Hybrid functionals based on a

screened coulomb potential. *The Journal of chemical physics,* 118, 8207 – 8215.

[19] Salpeter, E. E. and Bethe, H. A. (1951). A relativistic equation for bound-state problems. *Physical Review*, **84**, 1232.

[20] Tauc, J., Grigorovici, R. and Vancu, A. (1966). Optical properties and electronic structure of amorphous germanium. *Physica status solidi (b)*, **15**, 627-637.

[21] Mulliken, R.S., 1934. A new electro-affinity scale; together with data on valence states and on valence ionization potentials and electron affinities. *The Journal of Chemical Physics* **2**, 782 – 793.

[22] Butler, M.A., Ginley, D.S., 1978. Prediction of flatband potentials at semiconductor-electrolyte interfaces from atomic electronegativities. *Journal of the Electrochemical Society* **125**, 228 – 232.

[23] Behera, D., & Mukherjee, S. K. (2022). Optoelectronics and transport phenomena in Rb2InBiX6 (X= Cl, Br) compounds for renewable energy applications: a DFT insight. *Chemistry*, ***4***, 1044-1059.

[24] Iqbal, J., Ullah, H., Khishe, M., Azhdari, S. M. H., Ullah, R., & Iqbal, Z. (2024). New semiconducting K2MgSiH6 (H= cl & br) halides have been investigated via DFT approach; their mechanical, optical, and structural properties were studied in detail. *Scientific Reports*, ***14***, 23863.

[25] Voigt, W. (1928). A determination of the elastic constants for beta-quartz lehrbuch de kristallphysik, Terubner Leipzig **40** 2856–2860.

[26] Reuss, A. (1929). Berechnung der fließgrenze von mischkristallen auf grund der plastizitätsbedingung für einkristalle, *J. Appl. Math. Mech.* **9** 49–58.

[27] Hill, R. (1952). The elastic behaviour of a crystalline aggregate. *Proc. Phys. Soc. Sect. A* 65, 349.

[28] Mouhat, F., and Coudert, F. X. (2014). Necessary and sufficient elastic stability conditions in various crystal systems. *Physical review B*, *90*, 224104.

[29] Pugh, S. F. (1954). Relations between the elastic moduli and the plastic properties of polycrystalline pure metals. *The London, Edinburgh, and Dublin Philosophical Magazine and Journal of Science*, ***45***, 823-843.

[30] Gaillac, R., Pullumbi, P., & Coudert, F. X. (2016). ELATE: an open-source online application for analysis and visualization of elastic tensors. *Journal of Physics: Condensed Matter*, ***28***(, 275201.

[31] Abang, R.P., Musa, A., Solomon, R.A., Gidado, A.S., Hassan, S. First-principles investigation of structural, electronic, mechanical, optical, and thermodynamic properties of lead-free ksrx3 (x= f, cl, and br) halide perovskites for uv optoelectronic applications.

[32] Abdullah, D., So#, S.A., Tabook, M.A., Alkhaldi, N.D., Knani, S., Elaissi, S., Shah, A.U.I., Meyer, E.L. (2026). Probing energy device prospective: Inspecting thermoelectric, elastic, and optical response of strontium-based halide perovskites srcux3 (x= cl, br) via ab initio perception. *International Journal of Energy Research,* 6661890

[33] Dawood, F., Anda, M., and Shafiullah, G. M. (2020). Hydrogen production for energy: An overview. *International journal of hydrogen energy*, *45*, 3847-3869.